A FEASIBILITY EVALUATION OF X-RAY FLUORESCENCE EMISSION TOMOGRAPHY AND X-RAY LUMINESCENCE TOMOGRAPHY FOR REAL-TIME ASSESSMENT OF PHOTODYNAMIC THERAPY

BY

JONATHAN GEORGE

THESIS

Submitted in partial fulfillment of the requirements
for the degree of Master of Science of Nuclear, Plasma, and Radiological Engineering
in the Graduate College of the
University of Illinois at Urbana-Champaign, 2016

Urbana, Illinois

Master's Committee:

Associate Professor Ling-Jian Meng, Chair
Professor James F. Stubbins

ABSTRACT

Photodynamic Therapy (PDT) has found use in a wide-array of clinical applications such as in cancer and acne treatment. Photodynamic therapy, uses a photosensitive compound activated by a specific wavelength photon to produce cytotoxic oxygen species (either in free radical form or in singlet form). However, weak penetration of visible, infrared, and UV light into the body to activate the photosensitive compound significantly limits the use of PDT in cancer treatment. Additionally, PDT current lacks an effective dosimetry technique or means of quantifying the number of activated photosensitizers for investigative studies has proven difficult as well. Many researchers have delved into investigating x-ray induced PDT, which in combination of x-ray fluorescence computed tomography (XFCT), can produce a quantifiable therapeutic effect at greater bodily depths. This work demonstrates a novel combinatorial system of X-ray Fluorescence and X-ray Luminescence Computed Tomography (XLCT) to image LaF_3 and Y_2O_3 nanoparticles. A 3D XFCT/CT image of a mouse phantom conjugated with a NMR tube containing bromide and Y_2O_3 was produced. Additionally, a cross sectional imaging in XFCT/XLCT/CT of a mouse phantom with microcapillaries filled with $LaF_3:Tb^{3+}$ and $Y_2O_3:Eu^{3+}$ attached. The results demonstrated the plausibility of using a XFCT/XLCT/CT setup for monitoring therapeutic nanoparticles, but acquisition time and penetration depth issues will need to be addressed first.

ACKNOWLEDGEMENTS

I would like to thank my colleagues Andrew Groll, Luca Giannoni, Byung-Hui Yoon, and Dan Strat who partnered with me in the X-ray fluorescence project as a whole and contributed in the experimental setup and conducted the experimental procedure needed to verify the concepts discussed in this work. I would like to extend our appreciation to their supervisor, Professor Ling-Jian Meng from the University of Illinois at Urbana-Champaign as well as Professor Patrick La Riviere from the University of Chicago for their guidance and feedback through the effort presented in this work. Finally, additional thanks would like to be extended to the University of Illinois's Mechanical Engineering machine shop for manufacturing various parts needed in setting up the system.

TABLE OF CONTENTS

CHAPTER 1: INTRODUCTION 1
1.1 Objective 1
CHAPTER 2: BACKGROUND OF PHOTODYNAMIC THERAPY 3
2.1 Basic Principles of Photodynamic Therapy and Photochemistry 3
2.2 Cytotoxic Effects of Photodynamic Therapy 4
CHAPTER 3: BACKGROUND OF X-RAY FLUORESCENCE 5
3.1 A Brief Overview of Medical Based X-Ray Fluorescence 5
3.2 X-ray Fluorescence Analysis and X-ray Fluorescence Computed Tomography 6
3.3 The Competing Modalities and their Limitations 7
3.4 Limitations of X-ray Fluorescence Analysis and X-ray Fluorescence Computed Tomography 7
3.5 Addressing the Limitations 8
CHAPTER 4: BACKGROUND OF X-RAY LUMINESCENCE 9
4.1 Potential Medical Applications for X-ray Luminescence 9
4.2 An Overview of X-ray Luminescence and X-ray Luminescence Computed Tomography 9
4.3 The Competing Modalities and Their Limitations 11
4.4 Limitations of X-ray Luminescence Computed Tomography 11
CHAPTER 5: IMAGE FORMATION 13
5.1. Physically Defining a ROI using Apertures for XLCT and XFCT 13
5.2. Image Formation 13
5.3. Spectral and Image Correction via X-Ray CT 14
CHAPTER 6: MATERIALS AND METHODS 17
6.1. Overview of Experimental Design 17
6.2. Overview of Experimental Setup for Combined XFCT/CT 17
6.3. Experimental Procedure for Combined XFCT/CT 19
6.4. Experimental Procedure for Combined XFCT/XLCT/CT Setup 20
6.5 X-ray CT Setup 21
CHAPTER 7: RESULTS 23
CHAPTER 8: DISCUSSION 27
CHAPTER 9: FUTURE WORK 29
CHAPTER 10: CONCLUSION 31
REFERENCES 32

CHAPTER 1: INTRODUCTION

1.1 Objective

With the emergence of the anti-tumor breast cancer drug, abraxane, many research groups have begun investigating nanoparticles as a therapeutic agent for cancer treatment [1]–[3]. Nanoparticles conjugated with targeting ligands can accumulate at specific tumor sites to enhance therapeutic effects while minimizing damage to healthy cells [4], [5]. One specific type of nanoparticle-mediated cancer treatment gaining traction and clamor is photodynamic therapy (PDT), in which nanoparticles produce cytotoxic singlet oxygen upon irradiation of light [2].

However, traditional photodynamic therapy typically uses visible, near infrared, infrared, or ultraviolet light to induce singlet oxygen production in nanoparticles [2], [6]. However, this incident light lacks significant penetration depth limiting photodynamic therapy to a few millimeters to centimeters below skin. X-ray-activated photodynamic therapy techniques have gained much attention in the hopes of imparting therapeutic effects at greater depths than is possible with traditional photodynamic therapy [6], [7]. Interestingly, the very process that underlies X-ray induced therapeutic effects could also generate X-ray fluorescence (with metal-based nanoparticles) and/or X-ray luminescence (XL), which could be used to monitor the delivery and distribution of PDT agents and the subsequent therapeutic activation process. This leads to the possibility of using (XFCT) and X-ray luminescence computed tomography (XLCT) for monitoring therapeutic delivery during radiation therapy, which this work explores.

For instance, during the microbeam therapeutic delivery process, a highly collimated X-ray beam irradiates the object. The pre-administrated metal-containing nanoparticles (NPs)

preferably absorb the X-rays to produce therapeutic effects, either indirectly through mechanisms such as photosensitization [1, 2] and thermal ablation [8], or directly from radiation effects induced by low-energy secondary electrons (including Auger electrons) [9]. Resultant XF signals could determine the distribution of the NPs in the object and the absorption of X-ray energy through photoelectron interactions. The XL signals could provide quantitative information and indirect spatial mapping of the scintillation process induced by the X-ray irradiation of nanophosphors conjugated with photosensitizers. Finally, the micro-CT images provide structural details of the object for confirmation of the delivery of the beam to the target area. Combining these three imaging techniques would provide a unique tool for guiding therapeutic delivery with highly detailed spatial and functional information. This work examines the feasibility of such a combinatorial system.

CHAPTER 2: BACKGROUND OF PHOTODYNAMIC THERAPY

2.1 Basic Principles of Photodynamic Therapy and Photochemistry

Photodynamic therapy predominantly uses light as its means of operation for cancer treatment. A light-sensitive chemical agent known as a photosensitizer produces cytotoxic effect. Through unknown or various means (depending on the type of photosensitizer), the photosensitizer accumulates in the tumor location. Upon light irradiation, singlet oxygen is produced.

Singlet oxygen is a very excited and reactive molecule capable of interacting with biological relevant molecules found in membranes such as unsaturated lipids, cholesterol, tryptophan, histidine, and methionine [10]. Additionally, the singlet oxygen has a short lifetime, within 40 nanosecond, and a radius of action less than 20 nanometers [10]. This allows for a very specific targeting and localization with a tumor site.

Singlet oxygen is produced when light excites the photosensitizer, elevating it to and excited electron energy state. In this excited, several different mechanisms can occur. The sensitizer can return to ground state by emitting light in a process called fluorescence. The sensitizer can react directly with other molecules in tissue to produce radical intermediates. However, to produce the actual photodynamic effect, the energetic sensitizer would enter a triplet state through "intersystem crossing", in which the excited electron will go through a spin conversion to a lower excited state [10]. For an effective photosensitizer, this triplet state must have a long lifetime. In this triplet state, the sensitizer reacts with oxygen leading to singlet oxygen production as seen in Figure 2.1 [10].

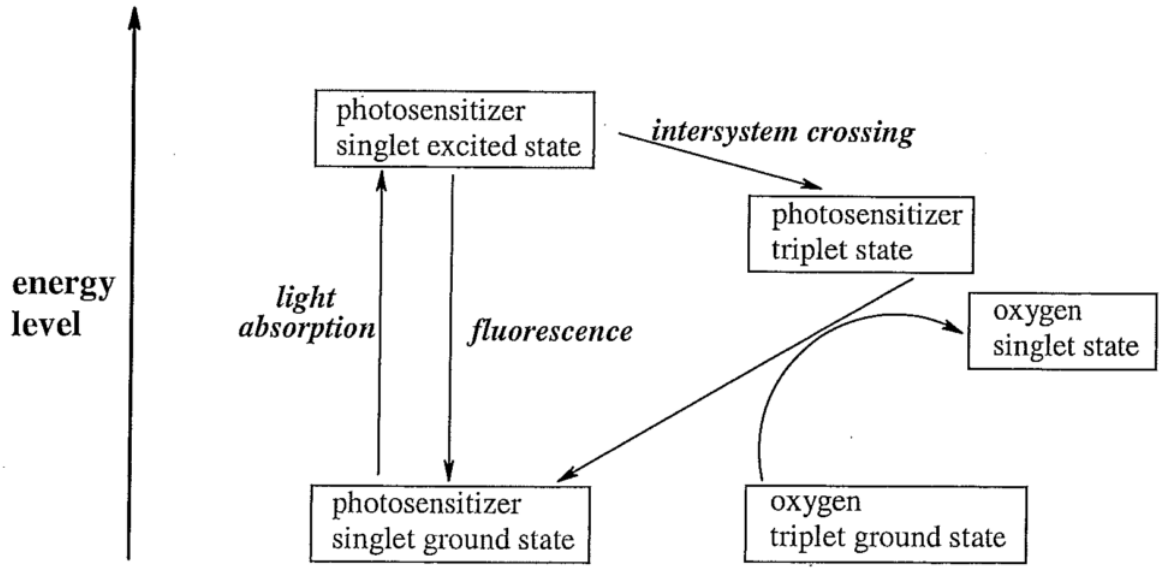

Figure 2.1 A diagram representation of singlet oxygen production via the photosensitizer [10].

2.2 Cytotoxic Effects of Photodynamic Therapy

Singlet oxygen can cause damage of membranes which causes swelling, bleb formation, and the halting of membrane enzymes. The membrane damage can cause the release of necessary proteins such as cytochrome c, which ultimately led to ATP depletion. Interestingly, PDT has varying potential for causing DNA damage as some sensitizing agents have a low probability of accumulating in cell nuclei while others can cause breakage in the double strands of DNA.

CHAPTER 3: BACKGROUND OF X-RAY FLUORESCENCE

3.1 A Brief Overview of Medical Based X-Ray Fluorescence

Much of the medical exploration of x-ray fluorescence based imaging comes from the mapping of key naturally occurring trace metals in biological samples. Being able to map these metals and their relevant processes *in vivo* can easily have numerous applications in clinical medicine. Such mapping can identify indicative pathologies of metals such as copper or magnesium in Parkinson's disease and other neurodegenerative disorders [11]. More specifically, recent research found a lack of copper within the substantia nigra and locus coeruleus of the brain in Parkinson's disease patients [12]. However, many of these studies and investigations are conducted using synchrotron radiation, and cannot be practiced *in vivo* due to dosage concerns.

To overcome this limitation, nanoparticles targeted to specific biological targets to enhance their output signal and reduce the need for a synchrotron source. For instance, recent work shows clinical ability of mapping naturally occurring trace metals includes the use of fluorescence nanoparticles coupled to ligands to serve as biomarkers on DNA [13]. With the growing study of the role of traces metals in genomics and proteomics, spatial resolute maps of the concentration of these trace metals have become critical [14]. Currently, X-ray fluorescence computed tomography (XFCT) has generated much attention as a potential means for mapping these trace metals since it does not require destructive sample preparation like those of SEM EDX, PIXE, and other methods. X-ray fluorescence analysis (XRF) has shown to be a viable method to acquire these concentrations of metals and markers of interest, but without providing spatial information. The amount of information acquired from X-ray fluorescence can be increased

significantly through the means of producing an image as done in X-ray Fluorescence Computed Tomography (XFCT), which can provide both spectral and spatial data.

3.2 X-ray Fluorescence Analysis and X-ray Fluorescence Computed Tomography

X-ray fluorescence analysis fundamentally depends on the ability for elements to produce signature X-rays when they interact with an initial primary X-ray. X-rays, in general, are produced from the atomic electron transitions and, therefore, contain characteristics specified by their element of origin. The typical stable atomic structure contains electron orbitals with correspond to specific distinct energy levels [15]. To remove an electron from its orbit, a certain level of energy, or binding energy, must be spent. If the removal of an inner orbital electron occurs, an outer electron may jump in to the new vacancy. This electron transition may produce a characteristic X-ray of energy equal to the difference of the two orbital binding energies. X-ray fluorescence occurs when a primary X-ray provides the initial energy required to remove an inner orbit electron, with the resulting electron transition producing the “secondary” fluorescent X-ray.

XRF utilizes the principle concept that the measured X-ray fluorescence intensity of a peak of an element relates to the concentration of the element in a sample [16]. This relation can be identified through a calibration procedure, which measures peak values of a known concentration of the element to be determined [17]. The XFCT modality produces images as well and typically incorporates a monochromatic X-ray beam to probe a rotating or translating sample. The incident X-rays induce characteristic fluorescence X-rays, which are used to construct a 3-D element distribution of the sample. Initial implementations of the system required the use of a high intensity synchrotron source to provide the monoenergetic X-rays. They also incorporate known

reconstructive techniques such as filtered-back projection or iterative reconstruction [18]. However, more recent studies have successfully used bench-top sources to quantify concentrations of lead in bone and gold nanoparticles in small tubes, albeit with relatively high concentrations [19], [20].

3.3 The Competing Modalities and their Limitations

Magnetic Resonance Spectroscopy (MRS) competes with X-ray fluorescence-based spectral analysis in their ability to quantize certain types of trace metals, such as gadolinium and iron, in a sample. MRS uses high strength magnetic fields in conjunction with a RF pulse at a specified frequency to examine particular in a region of interest [11], [12]. Although magnetic resonance based spectroscopy has pervasive use for *in vivo* use, they suffer from intrinsically low sensitivity with SNR value of 3:1 being commonly used [21]. This significantly low SNR is magnitudes less in order than fluorescence-based imaging and mass spectrometry [21].

Mass spectroscopy also has the capability to identify the chemical composition of trace elements in a sample. Mass spectrometry measures the mass-charge ratio to determine the presence of certain nuclei. However, mass spectrometry requires the use of vacuums and sample preparation, which often results in sample destruction. This makes mass spectrometry not applicable for *in vivo* application [14], [22], [23]

3.4 Limitations of X-ray Fluorescence Analysis and X-ray Fluorescence Computed Tomography

While these and other studies suggest that current XFCT/XRF systems can capably perform *in vivo* studies, they are also subject to a series of questions, such as the amount of contrast agents (e.g. metal nanoparticles) or the excessive dose needed to obtain acceptable images [3,4]. A Monte Carlo simulation study suggested that less than .5% by weight GNP

sample with 1 mGy dosage would provide poor image contrast with a current XFCT system [24][19]. These are mainly due to the intrinsically low interaction probability of the incident X-rays with the relatively low concentration of the metal content. Additionally, such studies show a limited sensitivity of 1μg/g [25].

3.5 Addressing the Limitations

With such limitations, can one map naturally occurring metals such as copper in mouse brain under *in vivo* settings be feasible, and can one do this with a benchtop X-ray source instead of a synchrotron X-ray source? In this work, we explore an alternative approach that relies on mechanical collimation and X-ray detectors to construct certain imaging geometries capable of mapping the elemental distribution of these trace metals without the need for full 3-D image reconstruction using benchtop X-ray sources. Earlier works by this group have demonstrated the plausibility of such imaging techniques without the use of computational image reconstruction techniques using synchrotron radiation from the Advance Photon Source [26]. By designing the aperture with a large open fraction (say 10% or more), one just needs to count how many fluorescence X-rays pass through the aperture, which will directly provide the elemental concentration values. Therefore, the metal concentration derived in this way is free of the so-called decoding penalty associated with 3-D imaging reconstruction, and could potentially have reduced statistical noise. By using high sensitivity imaging detectors and apertures with large open fractions, this approach would have the potential of offering the optimum sensitivity for quantifying the metal concentrations in 3-D samples.

CHAPTER 4: BACKGROUND OF X-RAY LUMINESCENCE

4.1 Potential Medical Applications for X-ray Luminescence

Quite similar to X-ray fluorescence, the rise of X-ray luminescence came from the need to combine the anatomical information of CT with information of the molecular processes that underlie various diseases. However, unlike X-ray fluorescence, X-ray luminescence requires the use of nanophosphors, scintillators, or the like to produce the visible light being imaged. However, XLCT has a poorer spatial resolutions at greater depths due to higher levels of scattering at greater depths [27]. This can be compensated for through information provided by XFCT, which maintains a good spatial resolution at greater depths

4.2 An Overview of X-ray Luminescence and X-ray Luminescence Computed Tomography

X-ray luminescence depends upon the process known as scintillation, in which X-rays are converted into visible light. These x-rays deposit energy into a target material causing the release of secondary electrons. The released high energy electrons cause further ionization downstream which ultimately results in the production of a large amount of low energy electrons. If the target is not scintillator, the energy of these electrons emits into heat. In scintillators, the electrons excite ion dopants into a temporarily stable excited electronic state. When this excited state returns back to ground, optical photons are released [28].

The emitted light typically falls within certain ranges of wavelengths; thus, certain nanophosphors or scintillators may emit green light while others could emit red. This allows for the targeting and separation of multiple nanophosphors injected into the body.

Combining this process with typical tomographic methods creates what is known as XLCT. In XLCT, a sample is irradiated by a pencil-collimated x-ray beams as it translates or rotates at set intervals in a geometry similar to that of first generation X-ray CT [28]. This is setup is shown in Figure 4.1. The nanophosphors are excited within a given irradiated volume emit visible light photons that are detected by an optical camera. The measured flux of these photons is proportional to the amount of nanoparticles in the irradiated volume. Various rotations and translations of both the motor and sample can ultimately produce a sinogram similar to that of conventional CT. Typical CT reconstruction techniques can then be applied to produce an image of nanophosphorous volume.

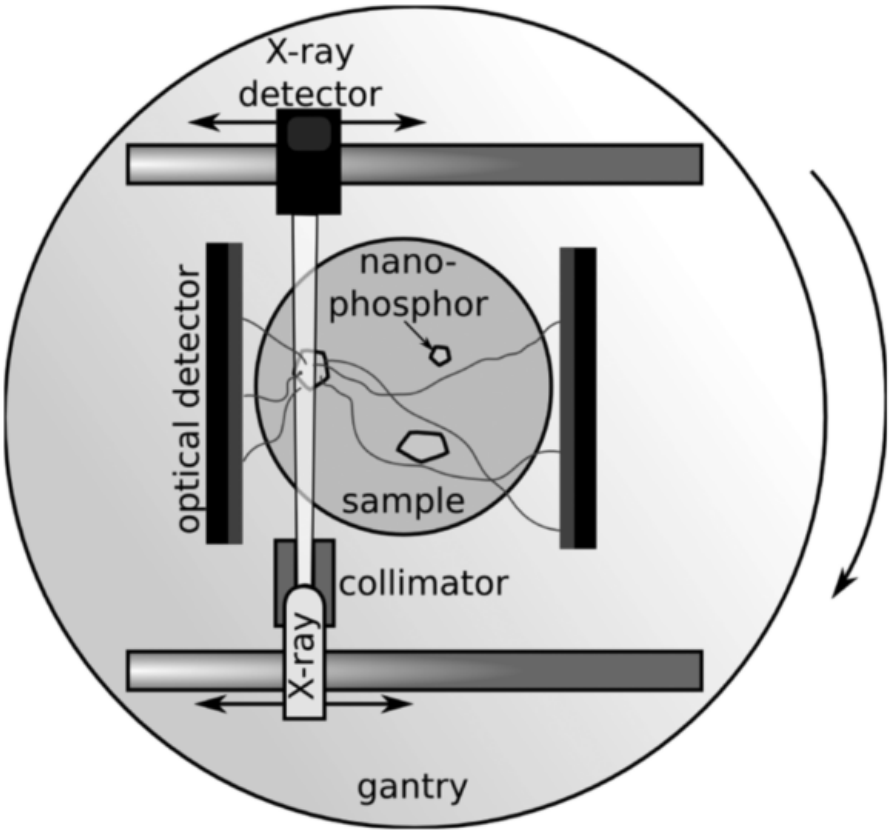

Figure 4.1—A first generation XLCT setup with a geometry similar to that of first generation X-ray CT [35]**.**

4.3 The Competing Modalities and Their Limitations

XLCT is in the realm of molecular imaging. The most clinically available molecular imaging tools would be Positron Emission Tomography (PET) and Single Photon Emission Computed Tomography (SPECT). Both these modalities require the use of radiopharmaceuticals that emit high energy gamma rays. These radiotracers accumulate in the specific regions of the body to monitor various biological processes such as glucose uptake. The high energy gamma rays can penetrate tens of centimeters of tissue, which is useful for whole body imaging [29]. These modalities also have high sensitivity and specificity, but have poor spatial resolution in the realm of millimeters when compared to other modalities.

Another optical imaging modality known as optical fluorescence imaging is the mainstream method for preclinical imaging. Fluorescence imaging utilizes optically fluorescent dyes that are taken up by cells. However, XLCT in comparison to this modality has greater spatial resolution at imaging depths. Optical fluorescence imaging is limited by the scattering of emitted optical light at these greater depths [28].

4.4 Limitations of X-ray Luminescence Computed Tomography

Many of the limitations of XLCT are akin to those of XFCT. Most current methodologies of image acquisition can be considered quite long for X-ray exposure. Additionally, since XLCT relies on probabilities of x-ray interaction with the nanophosphors and the probability of light emission. Only large concentrations (.2 mg/mL to 1 mg/mL) of nanoparticles/nanophosphors have been used in demonstrations of XLCT [27]. While some studies suggest that current XLCT systems can capably perform *in vivo* studies, such doses of nanoparticles could be deemed impractical for such studies [30]. Compare to XFCT, however, XLCT produces many more emission photons. At most, only one x-ray fluorescent photon can be produced by an incident x-

ray photon while several optical photons can be emitted in XLCT. However, XFCT emits higher energy x-ray which can penetrate at greater depths that optical photons. Thus, in comparison XLCT is still limited by depth as well.

CHAPTER 5: IMAGE FORMATION

5.1. Physically Defining a ROI using Apertures for XLCT and XFCT

If one could define the boundary of a ROI inside a sample with images from X-ray CT or other imaging techniques, then a specifically designed aperture would allow only fluorescence or optical X-rays from a linear segment of the ROI to register in our position sensitive X-ray detector. The system then scans the object across the beam. At any given beam position, a specific aperture will be placed in front of the detector to allow only those fluorescence X-rays from the ROI volume being irradiated in the sample. Given the known geometry, one can obtain a line integral of fluorescence X-rays through the ROI. By moving the object across the beam, one can derive a total concentration of the target metal within the ROI without running into the problem of 3-D image reconstruction from projections. Fig. 2.1a depicts this approach of imaging. The system incorporates an ultrahigh resolution spectrometer (the ANDOR camera in Figure 1a) coupled with the specially crafted set of apertures (shown in Figure 2.1c) placed perpendicular to the X-Ray CT detector (Paxscan 1313). While both of these Figures are specified for X-ray Fluorescence Computed Tomography, the same geometry is used for XLCT with the only difference being the exchange of the CCD with an EMCCD.

5.2. Image Formation

The volume-selective counting technique allows for acquiring spectral information, but also for image formation through mapping techniques. With the geometry of the system already predetermined, the pencil beam would interrogate the sample along a precisely known line. By translating the sample perpendicular to the beam in steps equivalent to the beam width, thus limiting the pixel width of the image to the beam width in one dimension, the system examines

an entire slice. By additionally translating in the vertical direction, the whole sample is interrogated, and a 3-D image can be obtained. Using the tapering of the aperture, the originating position of the fluorescence X-rays or luminescent phtons can be determined along the pencil beam's path. Thus, as seen in Fig 5.2 below, the final line segment is constructed by summing down the columns of the spectrometer. By simply placing these line segments next to each other, our final image is pieced together.

5.3. Spectral and Image Correction via X-Ray CT

The X-ray CT detector incorporated into the system does not only define the ROI within a sample, but also provide the X-ray attenuation information. Attenuation affects the gathered data in two ways: first by attenuating the incoming pencil beam, and secondly by attenuating the outgoing fluorescence X-rays. Without correcting for these sources of attenuation, an otherwise uniform sample would appear with a radial gradient with its minimum intensity at the point furthest away from both the pencil beam source and detector. The density information obtained through the X-ray CT system would correlate to relevant attenuation information that will help correct these attenuation effects. Many works have been published on the topic of attenuation correction, but a simple version of the correction is shown below [31], [32].

$$I(x,y) = I_0 * p * \left(\int_0^x \mu_a(u,y)d\,u\right) * \left(\int_\gamma^{\gamma_2}\int_{\alpha_1}^{\alpha_2}\int_0^{r_{2(\alpha,\gamma)}} \mu_f(\alpha,\gamma,r)d\,r\right)$$

Equation 5.1 I(x,y) is the measured intensity at pixel (x,y). I_0 is the initial incident beam intensity. p is the fluorescent coefficient, which functions as the probability of fluorescence occurring for a given mass of an element in a given volume. μ_a is the attenuation coefficient at incident beam energy at the given pixel position. Since the geometry is setup in such a way that the x-axis is parallel to the incident beam, u works as a dummy variable to note the distance the beam has traveled from 0 to pixel x. For the triple integral, the system is defined in spherical coordinates with α as the azimuthal angle, γ being the zenith, and the origin at (x,y). The angle integral limits are defined through the observed solid angle between the spherical origin and the detector space. The r limits are the boundaries of the sample. μ_f is the attenuation that occurs at the fluorescence energy at the given pixel position v.

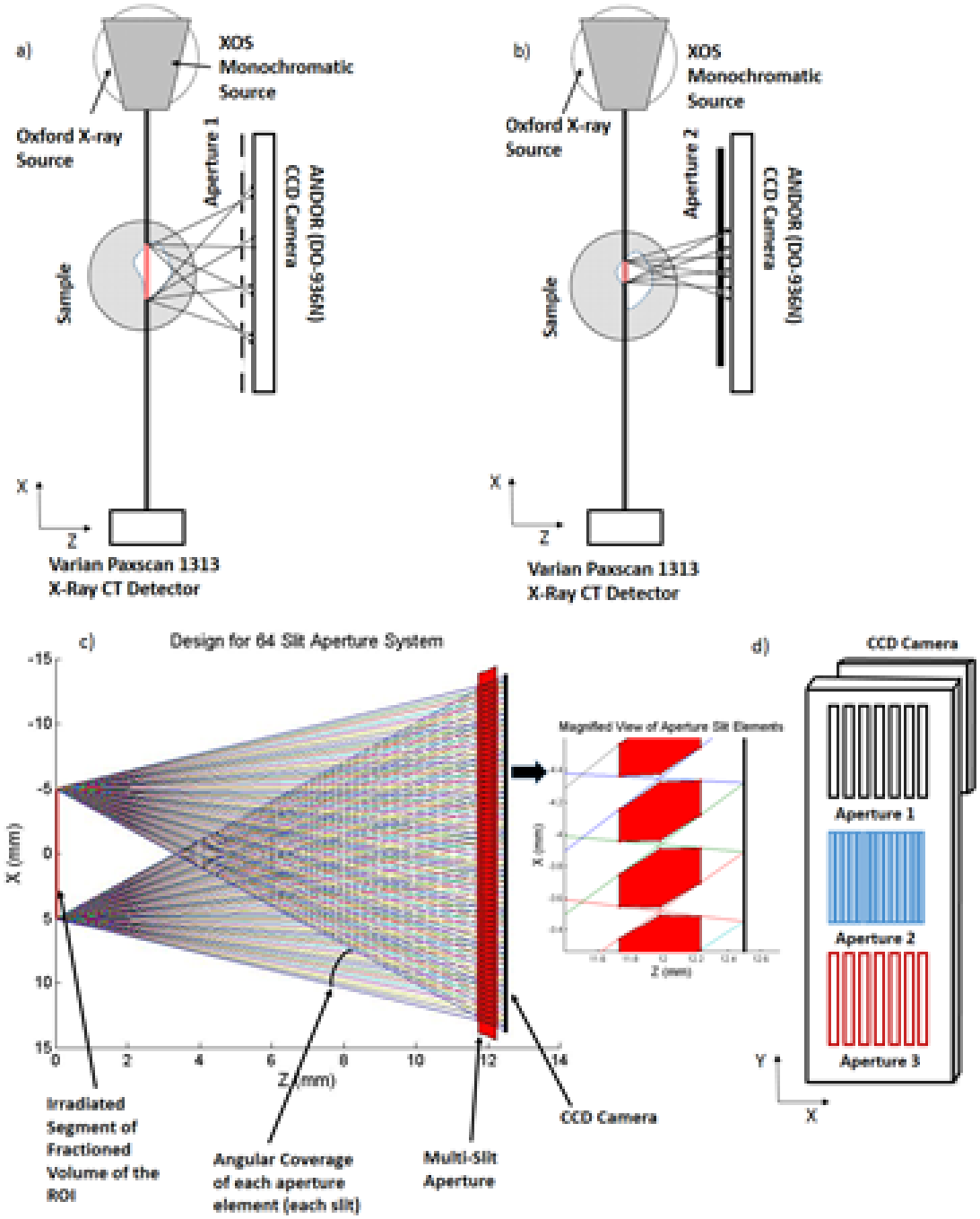

Figure 5.1: (A) The imaging system includes an X-ray CT system in conjunction with a CCD or EMCCD coupled with specially designed apertures. (B) The system translates the sample and various apertures can be used to achieve a highly sensitive photon count for a various specified segment of a ROI. (C) Every slit of the 64-slitted aperture shown is designed to examine the same 1 cm segment to provide a higher sensitivity count. (D) All the different apertures are to be produced on a single piece so that changing slits while scanning the sample becomes a matter of translating the aperture piece along the y-axis.

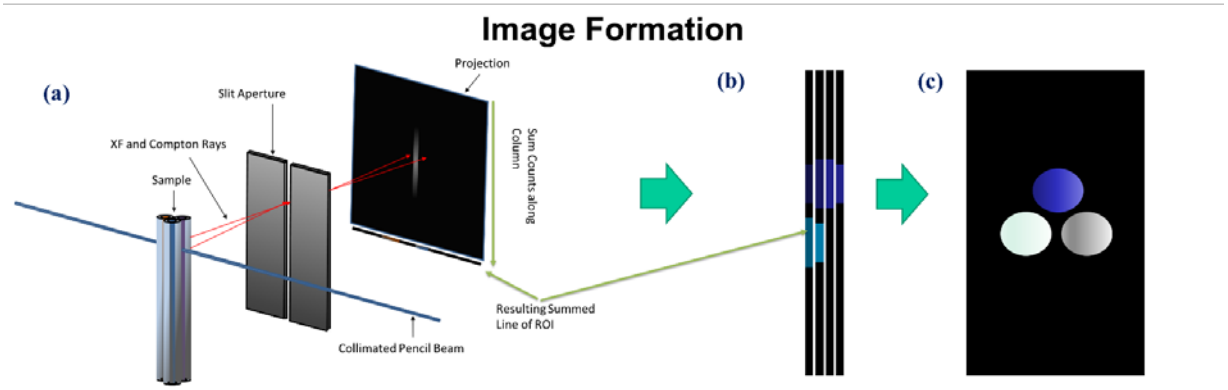

Figure 5.2: (A) When imaging, a linear segment of the ROI can be obtained by summing down the columns of the pixels of the projection as seen above. (B) Translating the sample via motors and then interrogating the new section and summing down the detectors column would produce a new line segment. When pieced together, these segments compose a 2D image or "slice" of the sample (C).

CHAPTER 6: MATERIALS AND METHODS

6.1. Overview of Experimental Design

Typical XFCT and XLCT image construction scans across a specimen as the specimen takes rotational steps. Sinograms are produced from this model of specimen interrogation through the use of non-position sensitive detectors. The sinograms are then used to reconstruct an image. The volume selective counting technique used in this work uses a direct mapping of sample via translation to acquire the image. The laboratory already contained much of the experimental setup needed to demonstrate the feasibility of a combined XLCT/XFCT setup. Our previous works in XFCT along with the aperture design dictated much of our geometrical layout [8]. Two different sets of studies and experiments were performed on two different but very similar setups. The first study simply demonstrated a combined XFCT/CT image of a nanoparticle filled tube attached to a 3D printed mouse phantom. The second study performed a combination of XFCT/XLCT/CT of a 3D printed mouse with two nanoparticle-filled microcapillary tubes attached.

6.2. Overview of Experimental Setup for Combined XFCT/CT

The system comprises of two X-ray sources, two detectors, four linear stage motors, and a rotational motor. The sample translates between two planes, upper and lower, with the upper plane containing X-ray CT equipment and the lower consisting of our XFCT design as seen in Fig. 3.

The X-ray CT plane consists of an Oxford Instruments polychromatic source—capable of emitting up to 50 keV photons—set across either a Varian Paxscan 1313 detector or a Andor Zyla 5.5. The flat panel detector encompasses 1024x1024 pixels of 127 μm x 127 μm in size

and covering a total area of 169 cm^2. The spectrometer is a CCD camera (Andor DO936N) containing a sensor area of 2048 × 2048 square pixels of 13.5 μm × 13.5 μm in size.

The lower plane consists of a monochromatic benchtop X-ray beam from XOS placed adjacent to a spectrometer coupled with a set of interchangeable multi-slit apertures. The system uses the set of motors to transfer the sample between planes as well as to properly scan our ROI. The four motors are capable of translation movement on the nanometer scale as well as precise rotation —a feature necessary as resolution of the mapping depends on the precision of the setup geometry. Figure 4 shows this setup.

Currently, the manufacturer specifies that the monochromatic X-ray source can focus unto a spot of 0.1 – 0.3 millimeter in diameter with an intensity of roughly send 17 keV at approximately $3x10^9$ Mo K X-rays per second passing through the cross section per second. Thus, this beam thickness will define up to two of the dimensions of our voxel while each aperture can specify the remaining dimensions.

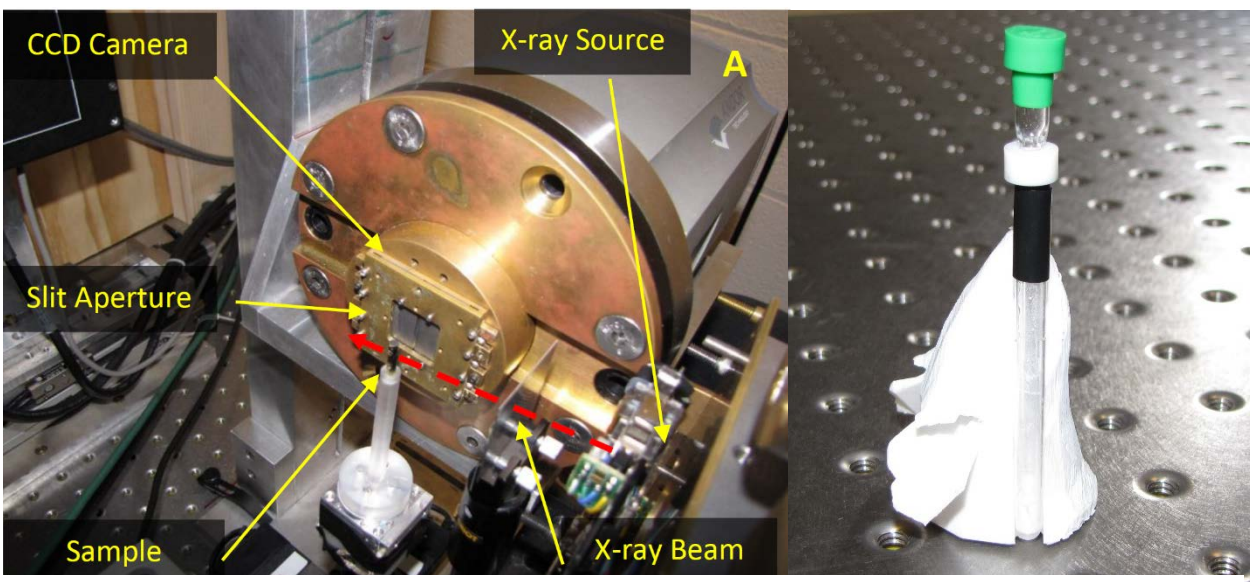

Figure 6.1: (A) The Geometry of the XFCT setup. The slit aperture is attached to the CCD and the sample is roughly 1 centimeter away from the slit. (B) The mouse phantom with the double tube attached.

6.3. Experimental Procedure for Combined XFCT/CT

For initial proof of concept, a double tube phantom was constructed containing Y_2O_3 nanoparticles in the outer tube and NaBr in the inner tube. The outer diameter of larger tube was 5 mm while the outer diameter of the smaller tube was 3 mm. The thickness of both the tube walls was 500 microns. The concentration of the Y_2O_3 was 118 mg/ml and the concentration of the NaBr was 172.6 mg/mL. This double tube was then attached to a mouse phantom, which serves as the sample.

The experiments used a single 100 micrometer slit aperture placed in front of the Andor CCD. Since the XOS source functions more akin to an incredibly narrow cone beam, the beam width at the sample's position must be determined. The Paxscan 1313 detector, placed at the sample position, resolved the beam width to be 100 micrometers.

Once the sample was setup, the sample was raised into the upper place in order to take an X-ray CT image. A X-ray CT image of the mouse was acquired in order to better define boundaries of the ROI, obtain an attenuation map, as well as to obtain a magnified view of the fish sample. For the image, a 50 keV voltage was applied to the tube as was as a 1.mA current.

After acquisition of the CT image, the motors lowered the sample to the fluorescence system. The pencil beam (XOS source) was set to send 17 keV at approximately 1.55×10^7 Mo K X-rays per second at the focal point of the beam. The Andor CCD was placed with a slit in front of the camera and set to acquire 1000 frames with a 10 second exposure per cross-sectional position. Accounting for readout time, this translates to about 3 hours per position with 50 positions being acquired. After 1000 frames were obtained, the motors translated the sample 100 micrometers in the direction away from the detector and towards the motor (as seen in Fig. 3).

After reaching the end of the defined boundaries, an image was directly mapped using earlier described methods.

6.4. Experimental Procedure for Combined XFCT/XLCT/CT Setup

The combined setup has a similar setup to the previous setup although with a few additional changes. The XOS source was replaced with the Xenocs source, which also has a 17.4 keV monochromatic source. It however also has a larger output of $3x10^9$ photons/s in the 100 micron diameter focal spot. Additionally, another transmission camera was added to the setup. The Andor Zyla CMOS camera contains 2560 by 2180 square pixels of 6.5 µm pitch.

Additionally, a Andor iXon electron multiplying charge-coupled device (EMCCD) was also used to acquire photons for XLCT. The Andor iXon contains 512 by 512 pixels of 16 µm square size. This sample was placed directly across from the CCD as seen in Figure 6.2A.

The sample also is a mouse phantom, but instead contains two micro capillary tubes filled with Y_2O_3:Eu^{+3} and the other filled with LaF_3:Tb^{+3}. These nanoparticles could not be dissolved

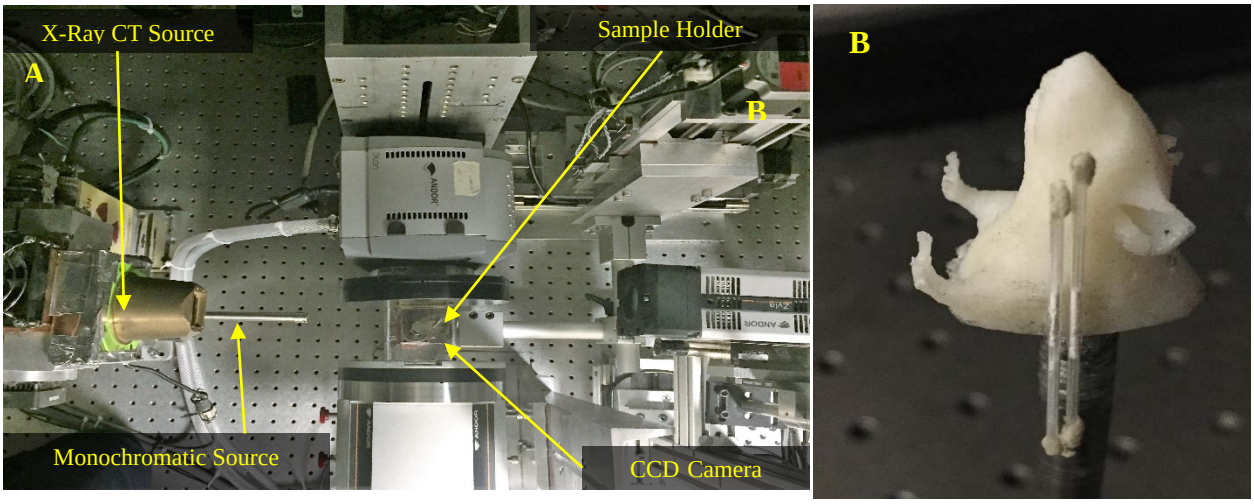

Figure 6.2: (A) The combined modality setup. The EMCCD (top-center) is set across the CCD in the image. (B) The mouse sample containing Y_2O_3 nanoparticles and LaF_3 nanoparticles and thus were filled into the microcapillary tubes as powders. These microcapillaries had an outer diameter of .0355 inches and an inner diameter of .0248”.

Aside from the inner and outer diameter differences the image acquisition method for the X-ray CT and XFCT was the same as the previous experiment. The microcapillaries on the mouse phantom were oriented in such a way that the incident beam would hit the nanoparticles without attenuation from the mouse and the emission photons would reach the CCD. However, only 15 positions were necessary to image the microcapillary tubes since their diameters were significantly smaller. 720 frames of 10 second exposure times were acquired for each position using the slit collimated CCD.

After XFCT and CT images were acquired, the setup then acquired XLCT images using the EMCCD. The EMCCD was also coupled to a 100 micron slit aperture. Only 600 .5 second frames were acquired for each of the 15 positions required to take the image.

6.5 X-ray CT Setup

In order for the X-ray CT system to function, the Paxscan 1313, the X-ray CT source, and the sample stage must be arranged in a known geometrical configuration. These geometrical parameters include the source to detector distance, Source to object distance, detector tilt, detector offset, sample stage offset, and central ray of cone beam location. All these parameters are necessary for successful and accurate X-ray CT reconstruction. 360 degree projections of a calibration phantom—each projection 1 degree apart—were incorporated into a preconditioned nonlinear conjugate gradient routine to determine the geometric prameters of the system. This calibration code was provided by a commecial company known as Xoran. The output of this data determined the parameters shown in Table 6.1 used in the experimental procedures for the mouse phantom as an example. The final CT reconstrution was performed via software called COBRA

purchased from the company known as EXXIM.

Table 6.1 The table depicts the geometric parameters used in the experiment procedure.

PARAMETER	DEFINITION	VALUE
SD	Source to Detector Distance	434.3035 mm
SO	Source to Object Distance	124.000 mm
TD	Detector offset in x-direction	-0.1157858 mm
TC	Distance between central ray and center-of-rotation	.1035698 mm
CS	Central ray position from center of detector in Y-direction.	0.1845173 mm
B	Detector Pivot	-0.01085245 radians

CHAPTER 7: RESULTS

The double tube phantom from the XFCT/CT experiment produced the spectrum seen below in Figure 7.1. The inner tube's bromide 11.22 keV Kα1 peak and 12.5 keV Kβ1 peak is clearly visible in the spectrum. Additionally, the ytrrium 14.96 keV Kα1 peak and 16.96 keV Kβ1 peak. Surprisingly, zinc 9.57 and 8.64 keV peaks also appeared in the spectrum. When isolating those energies in Figure 7.2, we find that they come from the glass.

Figure 7.2 shows the four energy isolated images of a single slice of the double tube. The gray scale in all 4 images is the CT image of the double tube. Figure 7.2A depicts the yttrium (green) within the double tube phantom. The yttrium was isolated by specifically selecting events registered on the CCD within the energy range of the yttrium peaks (as seen in Figure 7.1). Likewise, red in these images represents the bromide and the blue represents the zinc within the glass. In these images, the primary X-ray source comes in from the bottom and the CCD is

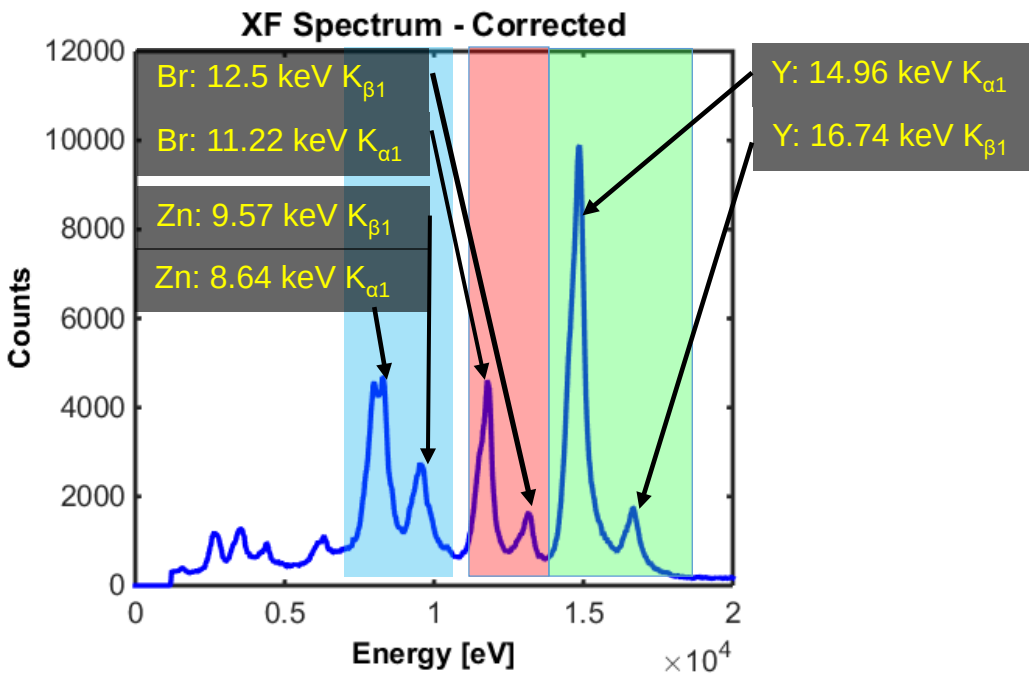

Figure 7.1- The spectrum obtained from the double tube mouse phantom. The Zinc peaks are from the glass of the NMR tubes used.

placed on the left. The yttrium does not produce a full-ring due to self-attenuation on the primary beam and emitted fluorescence. The bromide data shows the same effect. This can be corrected using CT data to apply an attenuation correction.

Figure 7.3 shows the 3D rendered image obtained from X-ray fluorescence with X-ray CT. The mouse phantom was imaged in its entirety while the fluorescence was only imaged in a small region of interest. Figure 7.3 follows the same color scheme as Figure 7.2, with bromide fluorescence depicted in red, yttrium in green, zinc in blue, and the gray scale representing X-ray CT data.

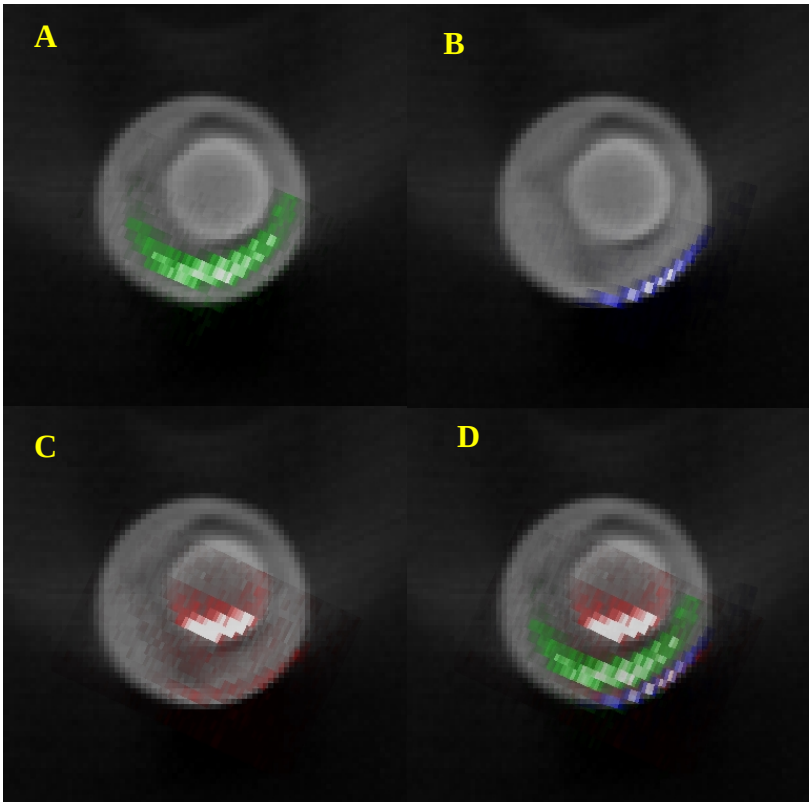

Figure 7.2: The gray scale portion of all these images are the ones obtained from X-ray CT. (A) The green represents counts found from yttrium fluorescence. (B) Zinc fluorescence from the glass was observed in blue. (C) The bromide fluorescence is represented in red. (D) A combination of all the energy isolated fluorescence using the earlier described color schemes.

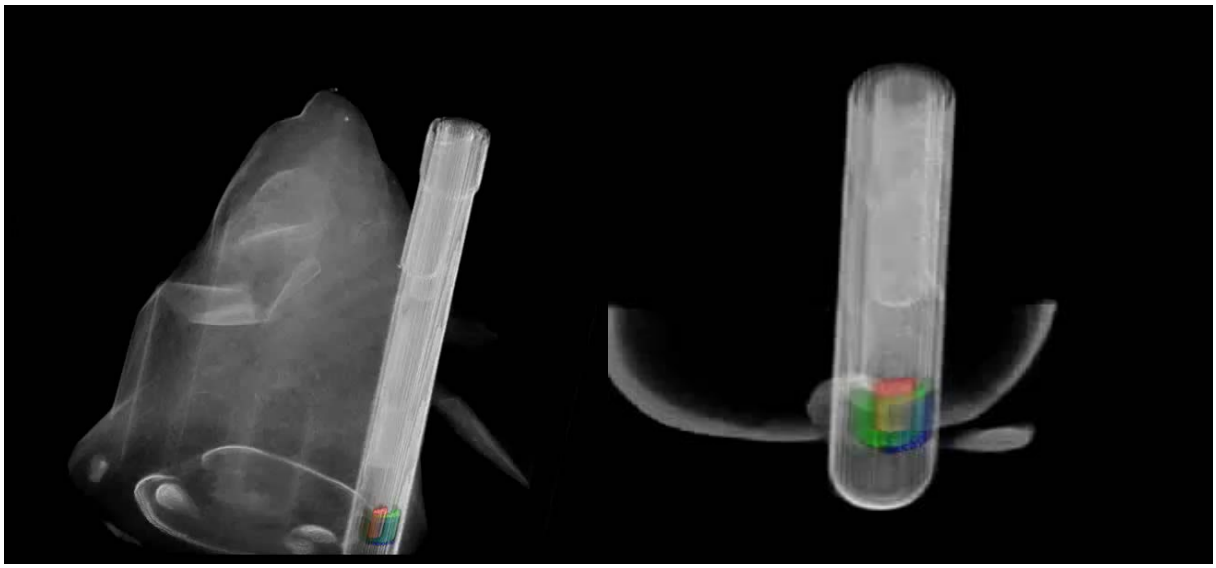

Figure 7.3: The gray scale portion of all these images are the ones obtained from X-ray CT. The green represents counts found from yttrium fluorescence. Zinc fluorescence from the glass was observed in blue. (C) The bromide fluorescence is represented in red. A combination of all the energy isolated fluorescence using the earlier described color schemes. The image on the left shows the full mouse and double tube phantom while the image on the right is zoomed in on the tube.

For the combined XFCT/XLCT/CT experiment, a spectrum as also obtained as seen in Figure 7.4. However, no lanthanum peaks were observed in the spectrum. Additionally, the 16.74 peak had some level of contamination from 17.4 keV Mo primary peak. Thus, it was not used in the energy isolated fluorescence image seen in Figure 7.5B.

Additionally, an XLCT image was also acquired using the previously described method. Luminescence from both the $LaF_3:Tb^{+3}$ and $Y_2O_3:Eu^{+3}$. In Figure 7.5A, x-ray luminescence of yttrium (blue) and LaF_3 (red) nanoparticles are depicted.

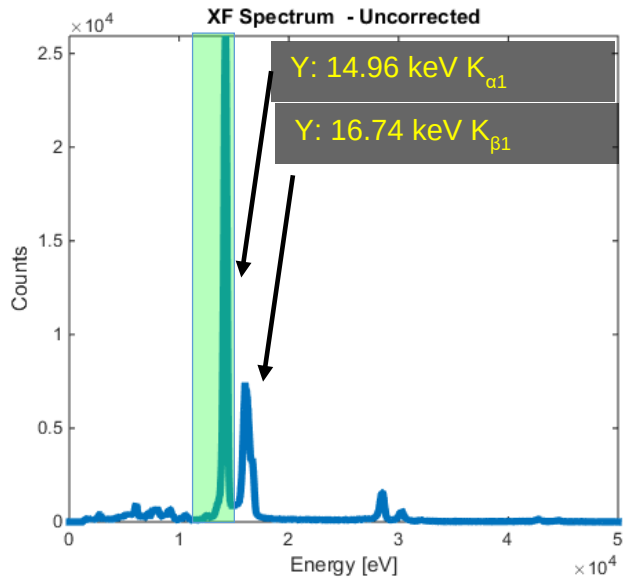

Figure 7.4: Irradiation of the LaF_3:Tb and Y_2O_3:Eu nanoparticles only resulted in the observation of yttrium peaks.

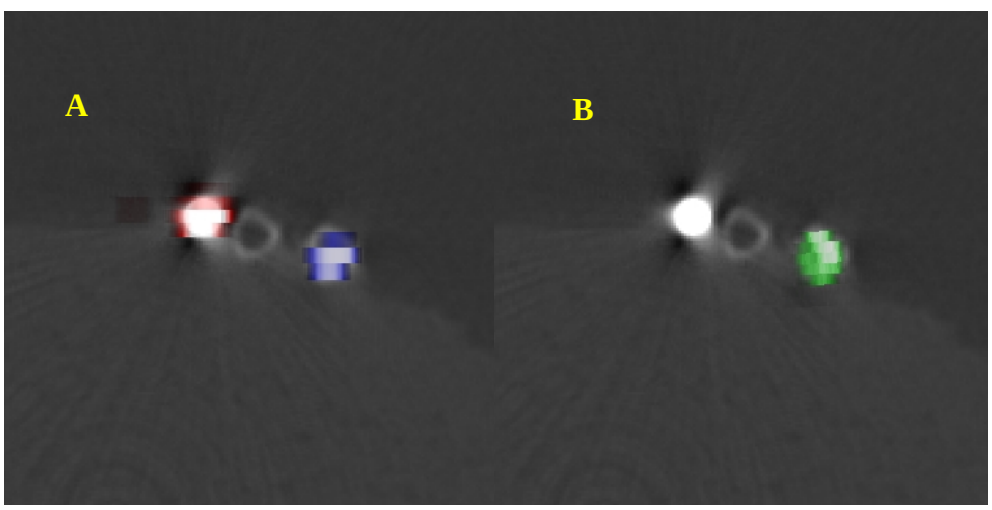

Figure 7.5: (A) XLCT image of a slice of the mouse phantom with LaF_3:Tb in red and Y_2O_3:Eu in blue . (B) XFCT image of the sample. Yttrium is in green, and the LaF_3 is not visible.

CHAPTER 8: DISCUSSION

The experimental work carried out in this work suggests that using a combined XFCT/XLCT/CT setup to monitor PDT may be possible. In spectra, yttrium and bromide were clearly resolved. Also, unexpectedly, zinc fluorescence was found in the glass of the nuclear magnetic resonance tubes. The images demonstrate the capability of using specified geometries in conjunction with aperture to create quantitative maps of a sample without reconstruction and its resulting decoding penalty. The experiments also depict the potential for producing 3D images by simply adding a vertical motor translation component to the same experiments. Regrettably, current acquisition times require a few days to obtain each of the specified slices. This currently prohibits the setup for any sort of *in vivo* use. Nevertheless, there are a few means to decrease acquisition times. These include attaching a multi-slit aperture onto the EMCCD and CCD, this would allow for a larger solid angle and thus would increase the overall sensitivity of the setup. Additionally, a more intense source would quickly reduce the necessary imaging time.

The images also show the significant effect of the attenuation of both internal fluorescence X-rays and the primary radiation source as well. Figure 7.2 most clearly demonstrates this effect as only half the expected circle of bromide appeared in the final image despite the uniformity in concentration within the tube. However, the highest fluorescence count occurs at the entry points of the primary X-ray beam. Attenuation-based correction factors from X-ray CT still need to be applied to achieve more accurate quantitative information.

Additionally, the Figure 7.4 and Figure 7.5 both show a lack of lanthanum in the fluorescence image and spectra. The k-edge of lanthanum is 38.9 keV, which is significantly higher than the 17.4 keV excitation energy of the primary beam. Thus, no K-edge fluorescence is expected from lanthanum. The lack of L-energy fluorescence from lanthanum ranged from 4 keV to 6 keV. This

may not have been observed due to a low emission yield and/or due to the energy not being penetrative enough to escape the sample.

However, Figure 7.5 does show a significant yield of light from both samples in the XLCT image. The larger the light yield, the more pronounced of a PDT effect would be expected in therapeutic settings. The ability to observe such a light yield is promising, but whether such a light yield would be observed in less ideal settings remains to be a question.

Despite these limitations in the results, the data suggests that such an imaging system technique can work for *in vitro* settings and has plausibility *in vivo* environments. A camera in conjunction with a single slit aperture acquired data from a sample placed in a known geometric setup. Through this known geometry, an image was produced for each sample by mapping each sample position. This exemplifies the major benefit of volume selective counting: the ability to generate 2-D or 3-D images without image reconstruction and its decoding penalty. Given long enough acquisition times, a higher intensity laboratory X-ray source, and/or a multi-slit aperture, a spectrum could be produced for every motor position or ‘pixel’ of the image showing the full benefit of the volume selective counting technique.

CHAPTER 9: FUTURE WORK

The focus of the future work in the current generation of the system will be on reducing the total acquisition time by increasing overall system, sensitivity, incorporating attenuation correction factors, determining minimum detectable concentrations of these nanoparticles, and exploring other nanoparticles. A proper method to correlate density and attenuate information to the X-ray fluorescence data has yet to be achieved, but other groups have made great strides and published works on correlating images from multi-modality systems [33], [34].

Acquisition time of the CCD can be considered the sum of the readout time and the total exposure time to acquire significant X-ray fluorescence information. With the readout time being inherent in the equipment, only the exposire time can be reduced. The group plans to reduce exposure time through two main means. Firstly, the Xenocs source can be replaced with an even more intense source such as a medical linear accelerator, increasing the X-ray interaction probability, and, therefore, the number of fluorescence X-rays produced. Since this would be in the radiation therapy setting, dosage is of less of a concern.

Aside from increasing the primary beam flux, the number of photons that reach the CCD can be improved by adjusting the detector's aperture. The effort presented in this work used a single-slit aperture, which attenuated a significant amount of photon information and underutilized the useable CCD surface area. By introducing additional slits that target the same sample segment as the single slit, exposure time can be drastically reduced as the sensitivity of the system increases in magnitudes of order. With such multi-slit aperture designs, the method for image formation would remain unaltered. Currently, designs for such aperture have already been created; however, and the authors are searching for a means to fabricate such intricately tapered apertures. Additionally, only one CCD or EMCCD detector was used in this experiment.

Greater sensitivity can be achieved by using a ring of detectors as seen in Figure 9.1. All these currently undergoing efforts would increase the sensitivity of the XFCT and XLCT system, potentially giving it the necessary foothold to entire *in vivo* research.

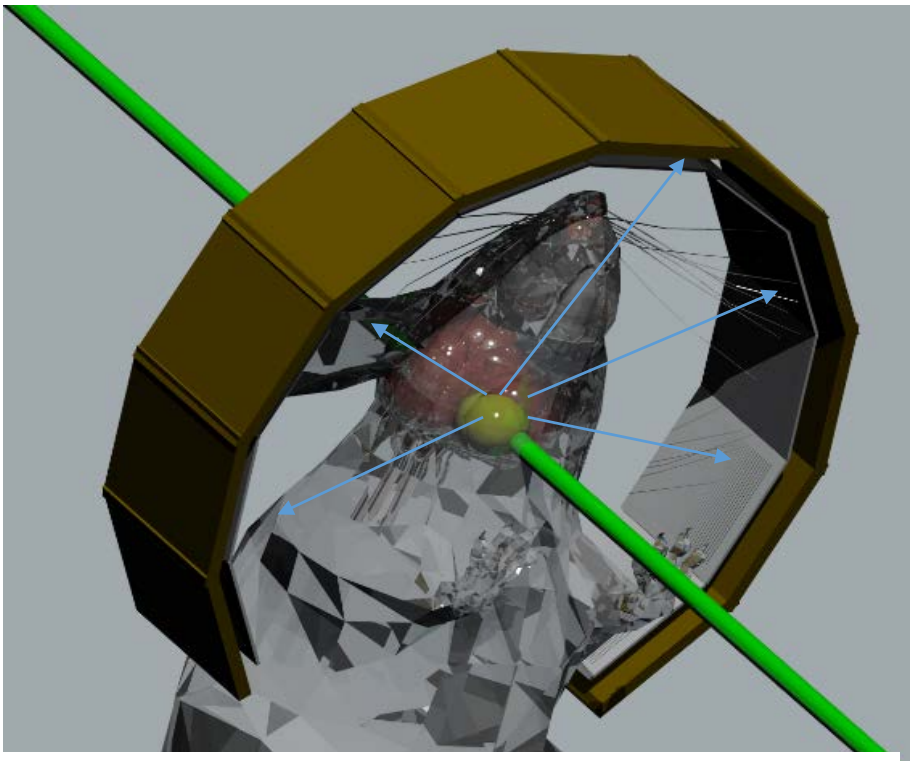

Figure 9.1:A full ring of detector coupled with apertures to increase the sensitivity of the XFCT or XLCT setup.

CHAPTER 10: CONCLUSION

In summary, this work explored the possibility of using a combinatorial system of X-ray fluorescence computed tomography (XFCT), x-ray luminescence tomography (XLCT), and conventional X-ray CT (CT) imaging to provide real-time information on the therapeutic delivery of photodynamic therapy nanoparticles. Two phantom studies were conducted too demonstrate the plausibility of such a system. The first study produced a combined XFCT/CT 3D image of a mouse phantom with a double tube containing NaBr and Y_2O_3 as well as a spectrum depicting the bromide and yttrium fluorescence peaks. The second experiment yielded a cross-sectional XLCT/XFCT/CT slice of two microcapillary tubes, containing $LaF_3:Tb^{3+}$ and $Y_2O_3:Eu^{3+}$, attached to a 3D printed mouse.

The results of these initial experiments show that conceptually using such a combinatorial system to monitor PDT could work, a few more questions need to be answers and some limitations need to be addressed. A minimum detectable concentration would need to be determined for these nanoparticles and system. Additionally, the current acquisition times are quite long to be performed for *in vivo* applications. Increasing sensitivity and reducing acquisition time can be achieved by using a ring of detectors attached to mult-slit apertures. Additionally, using nanoparticles with a higher K-edge could improve any penetration issues while using a strong flux source would also decrease acquisition time by producing greater luminescent and fluorescent yields. With these questions and limitations addressed, a combinatorial XFCT/XLCT/CT system could be seen monitoring the therapeutic delivery of PDT nanoparticles.

REFERENCES

[1] L. Ma, X. Zou, and W. Chen, "A New X-ray Activated Nanoparticle Photosensitizer for Cancer Treatment," *J. Biomed. Nanotechnol.*, vol. 10, no. 8, pp. 1501–1508, 2014.

[2] B. Ungun, R. Prud'Homme, and S. Budijon, "Nanofabricated upconversion nanoparticles for photodynamic therapy," *Opt. …*, vol. 17, no. 1, pp. 80–86, 2009.

[3] H. Chen, G. D. Wang, Y. J. Chuang, Z. Zhen, X. Chen, P. Biddinger, Z. Hao, F. Liu, B. Shen, Z. Pan, and J. Xie, "Nanoscintillator-Mediated X-ray Inducible Photodynamic Therapy for in Vivo Cancer Treatment," *Nano Lett.*, vol. 15, no. 4, pp. 2249–2256, 2015.

[4] S. Fokong, B. Theek, Z. Wu, P. Koczera, L. Appold, S. Jorge, U. Resch-Genger, M. van Zandvoort, G. Storm, F. Kiessling, and T. Lammers, "Image-guided, targeted and triggered drug delivery to tumors using polymer-based microbubbles.," *J. Control. Release*, vol. 163, no. 1, pp. 75–81, Oct. 2012.

[5] T. Lammers, W. E. Hennink, and G. Storm, "Tumour-targeted nanomedicines: principles and practice.," *Br. J. Cancer*, vol. 99, no. 3, pp. 392–7, Aug. 2008.

[6] S. Clement, W. Deng, E. Camilleri, B. C. Wilson, and E. M. Goldys, "X-ray induced singlet oxygen generation by nanoparticle-photosensitizer conjugates for photodynamic therapy: determination of singlet oxygen quantum yield," *Sci. Rep.*, vol. 6, no. October 2015, p. 19954, 2016.

[7] S. Kascakova, A. Guilani, S. Lacerda, A. Pallier, M. Pascal, E. Toth, and M. Regregiers, "X-ray-induced radiophotodynamic therapy (RPDT) using lanthanide micelles: Beyond depth limitations," *Nano Res.*, vol. 8, no. 7, pp. 2373–2379.

[8] Y. Jin, Y. Li, X. Ma, Z. Zha, L. Shi, J. Tian, and Z. Dai, "Encapsulating tantalum oxide into polypyrrole nanoparticles for X-ray CT/photoacoustic bimodal imaging-guided photothermal ablation of cancer," *Biomaterials*, vol. 35, no. 22, pp. 5795–5804, 2014.

[9] J. D. Carter, N. N. Cheng, Y. Qu, G. D. Suarez, and T. Guo, "Nanoscale Energy Deposition by X-ray Absorbing Nanostructures," *J. Phys. Chem. B*, vol. 40, no. 11, pp. 11622–11625, 2007.

[10] M. B. Vrouenraets, G. W. M. Visser, G. B. Snow, and G. A. M. S. van Dongen, "Basic principles, applications in oncology and improved selectivity of photodynamic therapy.," *Anticancer Res.*, vol. 23, no. 1B, pp. 505–22, 2002.

[11] B. F. G. Popescu, M. J. George, U. Bergmann, A. V Garachtchenko, M. E. Kelly, R. P. E. McCrea, K. Lüning, R. M. Devon, G. N. George, A. D. Hanson, S. M. Harder, L. D. Chapman, I. J. Pickering, and H. Nichol, "Mapping metals in Parkinson's and normal brain using rapid-scanning x-ray fluorescence.," *Phys. Med. Biol.*, vol. 54, no. 3, pp. 651–63, Feb. 2009.

[12] K. M. Davies, S. Bohic, A. Carmona, R. Ortega, V. Cottam, D. J. Hare, J. P. M. Finberg, S. Reyes, G. M. Halliday, J. F. B. Mercer, and K. L. Double, "Copper pathology in vulnerable brain regions in Parkinson's disease," *Neurobiol. Aging*, vol. 35, no. 4, pp. 858–866, 2014.

[13] M. Hossain, C. Wang, and M. Su, "Multiplexed biomarker detection using x-ray fluorescence of composition-encoded nanoparticles," *Appl. Phys. Lett.*, vol. 97, no. 26, p.

263704, 2010.

[14] R. Lobinski, C. Moulin, and R. Ortega, “Imaging and speciation of trace elements in biological environment.,” *Biochimie*, vol. 88, no. 11, pp. 1591–604, Nov. 2006.

[15] M. C. Miller, *X-Ray Fluorescence*. 2010.

[16] M. West, A. T. Ellis, P. J. Potts, C. Streli, C. Vanhoof, D. Wegrzynek, and P. Wobrauschek, “Atomic spectrometry update—X-ray fluorescence spectrometry,” *J. Anal. At. Spectrom.*, vol. 27, no. 10, p. 1603, 2012.

[17] B. L. Jones, N. Manohar, F. Reynoso, A. Karellas, and S. H. Cho, “Experimental demonstration of benchtop x-ray fluorescence computed tomography (XFCT) of gold nanoparticle-loaded objects using lead- and tin-filtered polychromatic cone-beams.,” *Phys. Med. Biol.*, vol. 57, no. 23, pp. N457–67, Dec. 2012.

[18] L. Boisseau, P. and Grodzins, “Fluorescence Tomography Using Synchrotron Radiation at the NSLS,” *Hyperfine Interact.*, vol. 33, pp. 283–292, 1987.

[19] M. Bazalova, Y. Kuang, G. Pratx, and L. Xing, “Investigation of X-ray Fluorescence Computed Tomography (XFCT) and K-Edge Imaging,” *IEEE Trans. Med. Imaging*, vol. 31, no. 8, pp. 1620–1627, 2012.

[20] L. H. Nie, S. Sanchez, K. Newton, L. Grodzins, R. O. Cleveland, and M. G. Weisskopf, “In vivo quantification of lead in bone with a portable x-ray fluorescence system--methodology and feasibility.,” *Phys. Med. Biol.*, vol. 56, no. 3, pp. N39–51, Feb. 2011.

[21] A. Webb, “Increasing the sensitivity of magnetic resonance spectroscopy and imaging.,” *Anal. Chem.*, vol. 84, no. 1, pp. 9–16, Jan. 2012.

[22] G. Münzenberg, “Development of mass spectrometers from Thomson and Aston to present,” *Int. J. Mass Spectrom.*, vol. 349–350, pp. 9–18, Sep. 2013.

[23] L. Krásný, R. Hynek, and I. Hochel, “Identification of bacteria using mass spectrometry techniques,” *Int. J. Mass Spectrom.*, vol. 353, pp. 67–79, Nov. 2013.

[24] L. Meng, N. Li, and P. La Riviere, “X-Ray Fluorescence Emission Tomography (XFET) With Novel Imaging Geometries—A Monte Carlo Study,” *Nucl. Sci. IEEE …*, vol. 58, no. 6, pp. 3359–3369, 2011.

[25] D. H. McNear, E. Peltier, J. Everhart, R. L. Chaney, S. Sutton, M. Newville, M. Rivers, and D. L. Sparks, “Application of quantitative fluorescence and absorption-edge computed microtomography to image metal compartmentalization in Alyssum murale.,” *Environ. Sci. Technol.*, vol. 39, no. 7, pp. 2210–8, Apr. 2005.

[26] G. Fu, L.-J. Meng, P. Eng, M. Newville, P. Vargas, and P. La Riviere, “Experimental demonstration of novel imaging geometries for x-ray fluorescence computed tomography.,” *Med. Phys.*, vol. 40, no. 6, p. 061903, Jun. 2013.

[27] C. Li, K. Di, J. Bec, and S. R. Cherry, “X-ray luminescence optical tomography imaging : experimental studies,” vol. 38, no. 13, pp. 2339–2341, 2013.

[28] M. Ahmad, G. Pratx, M. Bazalova, and L. E. I. Xing, “X-Ray Luminescence and X-Ray Fluorescence Computed Tomography : New Molecular Imaging Modalities,” vol. 2, pp. 1051–1061, 2014.

[29] E. Miele, G. P. Spinelli, F. Tomao, A. Zullo, F. De Marinis, G. Pasciuti, L. Rossi, F.

Zoratto, and S. Tomao, “Positron Emission Tomography (PET) radiotracers in oncology--utility of 18F-Fluoro-deoxy-glucose (FDG)-PET in the management of patients with non-small-cell lung cancer (NSCLC).,” *J. Exp. Clin. Cancer Res.*, vol. 27, p. 52, Jan. 2008.

[30] H. Chen, T. Moore, B. Qi, D. C. Colvin, E. K. Jelen, D. A. Hitchcock, J. He, O. T. Mefford, J. C. Gore, F. Alexis, and J. N. Anker, “Monitoring pH-triggered drug release from radioluminescent nanocapsules with X-ray excited optical luminescence.,” *ACS Nano*, vol. 7, no. 2, pp. 1178–87, Feb. 2013.

[31] T. Yuasa, M. Akiba, T. Takeda, M. Kazama, A. Hoshino, Y. Watanabe, K. Hyodo, F. A. Dilmanian, T. Akatsuka, and Y. Itai, “Reconstruction Method for Fluorescent X-Ray Computed Tomography by Least-Squares,” vol. 44, no. 1, pp. 54–62, 1997.

[32] J. P. Hogan, R. a. Gonsalves, and a. S. Krieger, “Fluorescent Computer Tomography: A Model For Correction Of X-ray Absorption,” *IEEE Trans. Nucl. Sci.*, vol. 38, no. 6, pp. 1721–1727, Dec. 1991.

[33] E. Tomography, H. Zaidi, and B. Hasegawa, “Determination of the Attenuation Map in,” *J. Nucl. Med.*, vol. 44, pp. 291–315, 2003.

[34] Y. Masood, Y.-H. Liu, G. Depuey, R. Taillefer, L. I. Araujo, S. Allen, D. Delbeke, F. Anstett, A. Peretz, M.-J. Zito, V. Tsatkin, and F. J. T. Wackers, “Clinical validation of SPECT attenuation correction using x-ray computed tomography-derived attenuation maps: multicenter clinical trial with angiographic correlation.,” *J. Nucl. Cardiol.*, vol. 12, no. 6, pp. 676–86.

[35] G. Pratx, C. M. Carpenter, C. Sun, and L. Xing, “X-Ray Luminescence Computed Tomography via Selective Excitation : A Feasibility Study,” vol. 29, no. 12, pp. 1992–1999, 2010.